AUTHOR	Rivasto E, Khan MZ, Wu Y, Zhao Y, Chen C, Zhu J, Huhtinen H, Paturi P
TITLE	Lattice defect induced nanorod growth in YBCO films deposited on an advanced IBAD-MgO template
YEAR	2020
DOI	https://www.doi.org/10.1088/1361-6668/ab9000
VERSION	Final Draft/AAM
CITATION	E Rivasto *et al* 2020 *Supercond. Sci. Technol.* **33**(7), 2020. https://iopscience.iop.org/article/10.1088/1361-6668/ab9000

Lattice defect induced nanorod growth in YBCO films deposited on an advanced IBAD-MgO template

E. Rivasto[1,2], M. Z. Khan[1,2], Y. Wu[3], Y. Zhao [3], C. Chen[4], J. Zhu[4], H. Huhtinen[1] and P. Paturi[1]

[1] Wihuri Physical Laboratory, Department of Physics and Astronomy, FI-20014 University of Turku, Finland

[2] University of Turku Graduate School (UTUGS), University of Turku, FI-20014 Turku, Finland

[3] School of Electronic Information and Electrical Engineering, Shanghai Jiao Tong University, 200240 Shanghai, Peoples Republic of China

[4] Shanghai Superconductor Technology Co. Ltd., 200240 Shanghai, Peoples Republic of China

E-mail: elmeri.o.rivasto@utu.fi

Abstract. We have studied the growth of self-assembled $BaHfO_3$ (BHO), $BaZrO_3$ (BZO) and $BaSnO_3$ (BSO) dopants in $YBa_2Cu_3O_{6+x}$ (YBCO) films grown on CeO_2 cap layered IBAD-MgO based metallic template by pulsed layer deposition process. The substrate induced defect formation and its impact on the growth of columnar-type of nanorods within the YBCO matrix is structurally investigated and their effect on critical current anisotropy is studied via molecular dynamics simulation model. We observed that the developed template greatly directs the growth mechanisms of different nanorods and thus modifies the critical current anisotropy of differently doped YBCO thin films.

1. Introduction

The exploitation of high temperature superconductors in practical applications is mostly limited by their fragile ceramic structure and power losses due to movement of vortices [1]. The first problem has been addressed by growing $YBa_2Cu_3O_{6+x}$ (YBCO) thin films on metallic templates enabling the production of long and flexible superconducting conductor cables that are practical especially in power transport applications [1]. These metal templates need to have texturized buffer layers, on top of which the well texturized YBCO film can be deposited, in order to obtain good superconducting properties. Several methods have been developed to create well-texturized buffer layers, such as rolling assisted biaxially textured substrate approach (RABiTS) [2, 3] or ion-beam assisted deposition method (IBAD) [4, 5]. The latter problem, related to voltage losses due to vortex motion, has been effectively addressed by introducing non-superconducting

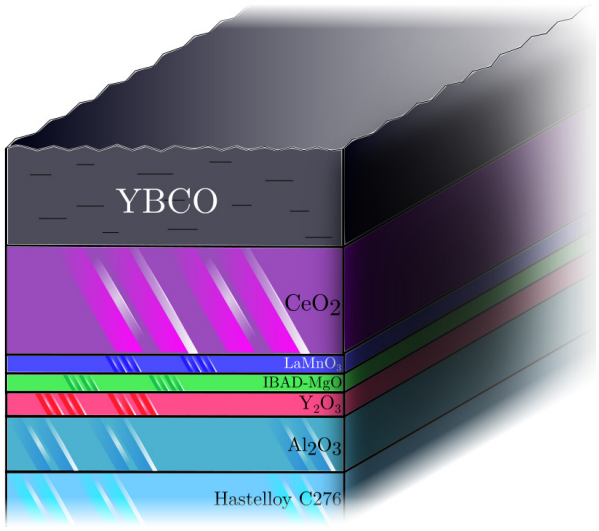

Figure 1. The layer structure of CeO_2-capped IBAD-MgO based template.

dopants within the YBCO matrix that pin the vortices. Recently, a remarkable topic of interest has been dopants that self-assemble themselves during the pulsed laser deposition (PLD) process in a columnar type of manner along the YBCO *c*-axis, having an effect on the critical current anisotropy by increasing its absolute value along the *c*-direction. Most commonly used dopants are $BaHfO_3$ (BHO) [6, 7], $BaZrO_3$ (BZO) [8, 9, 10] and $BaSnO_3$ (BSO) [11, 12], which form nanorod-type of structures in the PLD process along the YBCO *c*-axis of varying diameter between 2–12 nm [13, 14]. The formation and the properties of the nanorods, such as diameter, are theoretically well understood via behaviour of strain fields in the lattice of the thin film [14, 15]. The splay and fragmentation of the nanorods can be controlled by altering the growth temperature in the PLD process [8, 16]. However, the growth of these dopants on differently buffered metallic substrates is not well understood, especially how the substrate choice can affect the diameter, fragmentation and splay of the nanorods. Previous studies have shown degratation of the superconducting properties on films grown on buffered metallic templates when compared to films on single crystalline substrates [17, 18, 19], which is to be expected due to increased surface roughness of the metallic template which again increases the number of lattice defects in the superconducting film.

In this work, we have investigated the self-assembly of BHO, BZO and BSO nanoparticles within YBCO lattice deposited on an advanced CeO_2-capped IBAD-MgO based metallic template. We present a microstructural study together with critical current anisotropy measurements that are comprehensively discussed along with quantitative support of molecular dynamics simulations.

2. Experimental methods

The YBCO thin films, deposited from the targets doped with 4wt% of BHO, BZO and BSO, were grown on CeO_2-capped IBAD-MgO based template, as described in figure 1, via the pulsed laser deposition (PLD) method. The target materials were manufactured by a solid state ceramic method as described in [13, 20]. A 308 nm XeCl excimer laser was applied in the deposition process to irradiate the target by 1600 pulses with 5 Hz deposition rate and 1.3 Jcm^{-2} fluence, producing films with approximate thicknesses of 190 nm. The depositions were done at 775 °C with 0.175 Torr oxygen flow after which a 10 min oxygen treatment at 750 Torr pressure and 725 °C temperature was applied. More detailed descriptions of the PLD process are given in [13, 21]. To study the transport properties, 50 μm wide stripes were patterned to the surface of the film via wet chemical etching. Electrical contacts were made by using TPT HB05 Wire Bonder and aluminium wire. Transport measurements were done with the horizontal rotator option of Quantum Design PPMS system. The nanorod growth within the YBCO matrix was studied with Talos F200X transmission electron microscope (TEM) that was operated at 200 kV for which the cross-sectional samples were prepared by GAIA3 Gallium FIB-SEM system. Finally, the critical current angular dependency, $J_c(\theta)$, was simulated using molecular dynamics (MD) simulation in order to explain the measured $J_c(\theta)$ curves by pinning landscapes observed in TEM measurements. Details of the MD simulations are presented in [22].

3. Results and discussion

3.1. Structural analysis

Figure 2 presents the observed bright-field scanning transmission electron microscope (BF-STEM) images among with selected area electron diffraction (SAED) and high-resolution transmission electron microscope image (HRTEM) of film-substrate interface of BHO, BZO and BSO doped YBCO samples. A summary of the obtained results is presented in table 1.

A lot of variation can be observed in the assembly of BHO nanoparticles as seen in figure 2(a). The majority of the formed nanorods are fragmented and bent while some of them are somewhat long and *c*-axis oriented with an average diameter of 4 nm. Despite this and the large lattice mismatch of 8.85% between YBCO and BHO along the *ab*-plane, the obtained SAED image suggests epitaxial relationship between YBCO and BHO. Stacking faults are not observed. The detailed structure of the CeO_2-YBCO interface, presented in figure 2(c), shows that both the YBCO and BZO particles grow epitaxially on the CeO_2 surface without signs of interface reactions.

From figure 2(d), one can observe that the BZO nanoparticles have assembled themselves in columnar manner along the YBCO *c*-direction. These observed nanorods are approximately 5 nm in diameter and penetrate through the whole film without any significant splay or fragmentation. In addition, great number of stacking faults in the

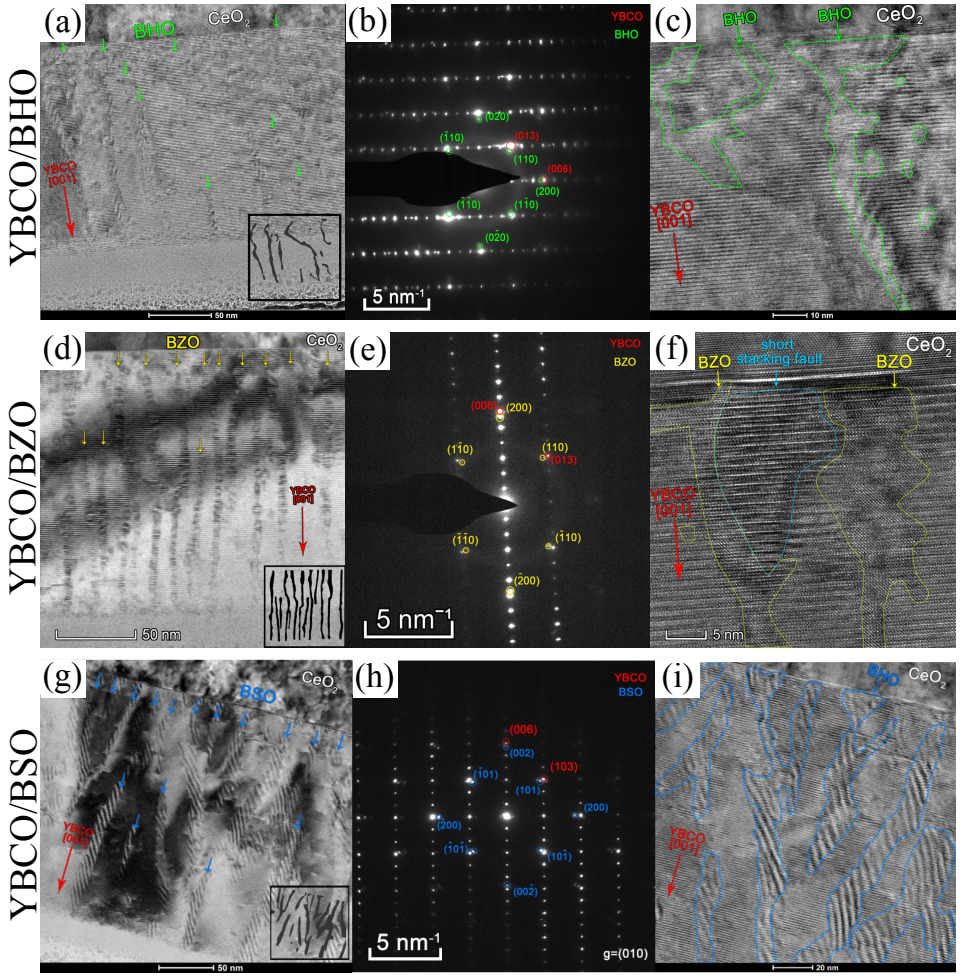

Figure 2. A bright-field scanning transmission electron microscope (BF-STEM) images, selected area electron diffraction (SAED) with identified intensity maxima and high-resolution transmission electron microscope image (HRTEM) of the film-substrate interface for (a)-(c) BHO, (d)-(f) BZO and (g)-(i) BSO doped YBCO. The green, yellow and blue arrows indicate the initial positions of nanorod growth while the red arrows indicate the (001) direction (c-axis) of the surrounding YBCO lattice.

bulk YBCO between different BZO nanorods can be observed. The SAED image in figure 2(e) indicates epitaxial relationship between YBCO and BZO, i.e., cube on cube growth, YBCO(001)⟨010⟩/BZO(100)⟨010⟩, despite their large lattice mismatch of about 8.28% along the YBCO ab-plane. This can be associated with a large accommodated strain at the coherent interface.

As was the case with the BHO nanorods, a lot of variation can also be observed in the growth of the BSO nanorods as some of them grow smoothly through the whole film while some are highly splayed and fragmented, as seen in figure 2(g). The BSO nanorods have approximately a constant diameter of 8 nm. According to the SAED image in figure 2(h), the BSO grows epitaxially within the YBCO lattice without any interface reactions between BSO and CeO_2 surface, i.e. YBCO(001)⟨010⟩/BSO(100)⟨010⟩, under a lattice

Table 1. A summary of the obtained BF-TEM results for different dopants.

	Diameter (nm)	Splay (°)	Fragmentation	Stacking faults
BHO	4	∼ 5–10	A lot	No
BZO	5	∼ 0	No	Yes
BSO	8	∼0–10	Some	Yes

mismatch of 6.85% along the YBCO *ab*-plane. Stacking faults can also be observed.

In our previous works, all of the associated dopants have been observed to form both long and *c*-axis oriented nanorods within YBCO on single crystalline $SrTiO_3$ (STO) substrate under similar deposition conditions with larger diameters of 4 nm, 7 nm and 12 nm for BHO, BZO and BSO, respectively [23, 14]. Interestingly, in this case only the BZO nanorods show similar *c*-axis oriented growth within the YBCO matrix as observed for single crystalline substrate, although even in this case the nanorod diameter is observed to be significantly smaller.

A factor that can degrade the growth of the nanorods is the increased number of lattice defects, such as twin boundaries and stacking faults, within the YBCO lattice grown on metallic templates. We have earlier observed that the 2θ and ϕ peaks in the XRD measurements are significantly broader in films grown on metallic templates when compared with similar films on single crystal substrates [13, 19]. The 2θ and ϕ peaks were 1.5 and 2.8 times broader, respectively, on the particular metallic template studied in this work. Broad 2θ peaks indicate increased presence of strain and other defects in the YBCO lattice while the broad ϕ peaks are associated with the presence of low angle grain boundaries and variation in the in-plane distribution of YBCO grains [24, 25].

The YBCO *c*-axis alignment of the nanorods has been theoretically shown to be related to the local strain in the vicinity of the nanorods which is characterized by the ratio f_1/f_3, where f_1 and f_3 are the lattice mismatches between YBCO and the dopant material along the *ab*-plane and the *c*-axis, respectively [14]. For *c*-axis oriented growth of the nanorods, this particular ratio needs to be above 1.0 and the higher the ratio is, the better the nanorods align themselves along the YBCO *c*-axis [14]. By using the theoretical lattice parameters for YBCO, BHO, BZO and BSO, the corresponding ratio can be found to be around 1.1 for all the dopants, which is just barely the ratio needed for the good *c*-axis alignment of the nanorods. Thus the nanorods are very sensitive to the variation of the lattice parameters in the YBCO, namely the texture imperfections and low angle grain boundaries, which are present in large amounts especially in the metallic templates. This suggests, that the large number of lattice defects is essentially the reason why nanorods do not grow as well along the YBCO *c*-axis on metallic templates as on single crystalline substrates. This correlation between the texture imperfections and nanorod growth has already been observed in [19], where pure and BZO doped YBCO was grown on three different metallic templates and the well *c*-axis aligned nanorods were only observed on a template, which is also the same CeO_2-capped template studied in this work, which had the lowest $\Delta 2\theta$ and $\Delta\phi$ values. For this particular template, these

values are approximately the same between undoped and BZO doped films, suggesting that the nanorod growth is particularly governed by the lattice defects in the YBCO and the lattice defects are not, in particular, formed due to the formation of the nanorods. The size of the nanorod has been proposed to be determined by the strain decay inside the nanorods [15]. This would suggest, that the observed decreases of the nanorod diameters in films on the metallic templates are also related to the distorted growth of the YBCO between them, which alters the strain decay.

The fact that we observed dramatic differences in the alignment of different nanorods, despite the similar growth conditions, suggests that something in PLD process itself affects the growth of the nanorods. We argue that the distorted growth of BHO and BSO nanorods is related to the unoptimized deposition temperature or too high growth rate that may limit the diffusion of the Hf and Sn atoms in the growth process [8, 16]. The growth temperature for our PLD system has previously been optimized only for BZO nanorods on the same metallic template used in this work but in the case of single crystalline substrate relatively good nanorod growth has been observed also for BHO and BZO at the very same growth temperature [23, 13]. This suggests that the nanorod growth is much more sensitive to temperature on CeO_2 template than on a single crystalline substrate.

3.2. Critical current anisotropy

Figure 3 presents the shapes of the experimentally measured $J_c(\theta)$ curves in various magnetic fields for all three samples. In the case of the BHO doped sample, no clear *c*-axis peak is visible, even in the high field range, which can be associated with the BF-TEM results, according to which the BHO nanorods are splayed, fragmented and in general very poorly arranged [16]. A good indication for the lack of *c*-axis oriented pinning can also be seen by comparing the absolute values of J_c along the *c*- and *ab*-directions. The absolute J_c is always much higher along the *ab*-directions compared with the *c*-direction due to the dominating effect of intrinsic $J_c(\theta)$ anisotropy of YBCO. In order to get more quantitative argument that the fragmentation and splay of the nanorods actually destroy the *c*-peak, we ran MD simulations with two different configurations, one of which contained only solid and YBCO *c*-axis oriented nanorods while the other had four times fragmented nanorods that were splayed randomly at maximum of 10° angle. The corresponding simulated *c*-axis peaks are presented in figure 4(a), where one can observe almost complete disappearance of the *c*-peak as the nanorods get fragmented. This is also in line with our previous computational study presented in [26], where similar type of tendency was reported. This is simply due to weaker pinning of the partially trapped vortices in the splayed and fragmented nanorods. These results quantitatively verify our previous intuitive statement about why we do not observe *c*-axis peak experimentally for BHO doped YBCO. Also, as seen in figure 3(a), the BHO doped YBCO has clearly the lowest absolute values of critical current, which can be associated with the poor growth of BZO nanorods that disturbs the surrounding YBCO lattice, thus

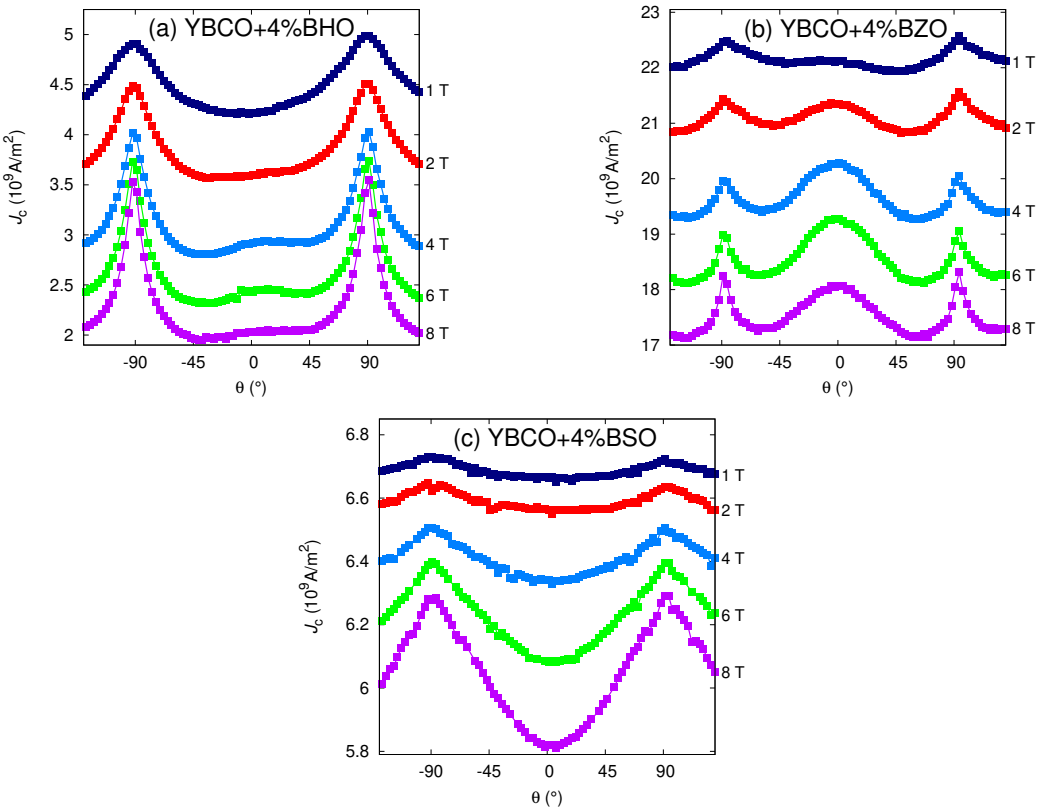

Figure 3. (a)-(c) The experimentally measured shapes of the $J_c(\theta)$ curves at various magnetic fields at 40 K for BHO, BZO and BSO doped samples, respectively. The zero angle is along YBCO c-axis.

weakening the superconducting properties of the sample. The experimentally measured broad ab-peak, that sharpens as the field is increased, indicates the presence of pinning sites that become effective at higher angles. According to our previous computational study [23], the large amount of effective pinning sites is indicated particularly by the sharpening of the ab-peak as the field is increased to 8 T, where the matching field along the ab-direction seems not have been exceeded yet. Notice, that the number of vortices is highly reduced in the ab-direction due to much smaller cross-sectional area that the magnetic field penetrates. Since ab-plane oriented stacking faults were not observed in the BF-STEM measurements, the vortices must become effectively pinned to the bent parts of the BHO nanorods at high angles. Vortex pinning in the associated pinscape of BHO is schematically illustrated in figure 5.

In the case of BZO, a clear c-peak, which gets more pronounced relative to the ab-peaks as the field is increased, can be observed. This is also the only sample in which the absolute value of J_c along the c-axis exceeds the corresponding value along the ab-directions. This is associated with strong c-axis oriented pinning due to straight, solid and well aligned BZO nanorods within the YBCO matrix as observed in the BF-TEM images. The simulated $J_c(\theta)$ curves in figure 4(a) support this argument quantitatively,

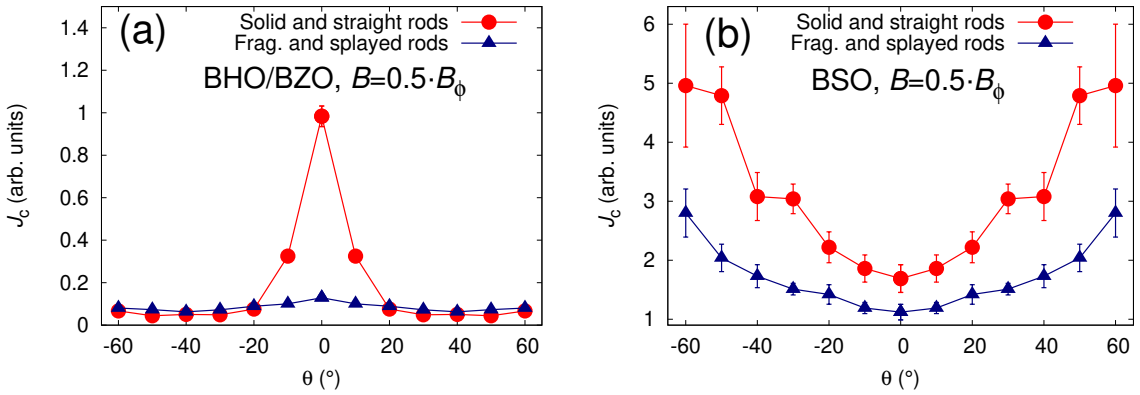

Figure 4. Simulated $J_c(\theta)$ points with standard errors for (a) solid and YBCO c-axis oriented nanorods of 4 nm diameter corresponding to 4% doped BHO and BZO as well as similar but four times fragmented nanorods with random splay of maximum 10° and (b) solid and YBCO c-axis oriented nanorods of 8 nm diameter corresponding to 4% doped BSO as well as similar but two times fragmented nanorods with random splay of maximum 10°.

as a high intensity c-peak can be observed namely with solid YBCO c-axis oriented nanorods. The good growth of BZO within the YBCO matrix is manifested by extremely high absolute values of J_c compared with all other dopants. Similarly with the previous BHO doped case, the ab-peak of the BZO doped sample also sharpens as the field is increased. Unlike in the case of BHO though, for BZO doped sample this is only due to the the presence of effective stacking faults. In this case, the absolute value of the ab-peak is significantly decreased at higher fields indicating the exceeding of the matching field. Thus, with the help of our previous computational study [23], we conclude that the stacking faults in the BZO doped sample are not that high in number, or as effective, as the bent BHO nanorods discussed in the previous case. This is in line with the BF-TEM results, where short stacking faults was observed only for BZO and BSO doped samples. Again, vortex pinning in the associated pinscape of BZO is schematically illustrated in figure 5.

For BSO doped films, the c-peak is completely absent even at high field range despite the relatively well c-axis oriented nanorods observed in the BF-TEM image of figure 2(g). This rather counterintuitive result was further investigated by running two simulations with 8 nm diameter nanorods, one of which had solid c-axis oriented nanorods while the other maximum of 10° randomly splayed and two times fragmented nanorods. The simulated c-peaks are presented in figure 4(b), where even in the case of solid c-axis oriented nanorods no c-peak is observed. This is perfectly in line with the experimental results. As explained in the previous cases, the sharpening of the ab-peak as the field increases indicades the presence of great number of stacking faults, which is supported by the BF-STEM images.

Similar result has been observed in our previous computational work [23], where

we concluded that the absence of the c-peak is due to the fact that the number of nanorods is reduced as their diameter is increased, as the dopant concentration is kept constant. Due to reduced number of the large BSO nanorods, the probability to pin the vortex along the c-direction is decreased. As the angle of the applied field increases, the vortices are much more likely to come across a nanorod and, due to their high pinning force, the vortices can still get strongly pinned to the nanorod, despite the fact that at higher angles only partial vortex pinning is observed. Interestingly, in our previous works [13, 23], when the 4% BSO doped YBCO film has been deposited on single crystalline substrate under similar growth conditions as in here, clear c-axis peaks have been observed. This has to be related to the much more solid and larger diameter nanorods that we have previously observed in the BF-STEM measurements in [23]. For the large diameter nanorods, the fragmentation seems to have more pronounced effect on the decreasing of the c-peak.

An alternative explanation for the missing c-axis peak can be that the density of the dopant material may vary substantially from the dopant density of the PLD target. Thus, in the experimentally measured films the nanorod density can be significantly higher when compared with the simulations. This has already been computationally verified in our previous work [23], where increasing the concentration of large diameter nanorods up to 8% suddenly produces a clear c-axis peak that was not observed at any lower concentrations. Thus we also argue, that under the same deposition conditions, the density of the BSO nanorods might be substantially lower when grown on buffered metallic template than on the single crystalline substrates. Qualitatively, this seems to be the case when comparing the BF-STEM image of figure 2(g) to the corresponding one presented in [23] although this cannot be considered very reliable evidence due to small area of where the images were taken. This would explain why we do not observe c-peak even in the solid nanorod case in the simulated $J_c(\theta)$ curves presented in figure 4(b).

The observed distortions in the growth of the BSO nanorods is manifested by relatively low absolute values of critical currents. The absolute values of critical currents of the BSO doped samples are still substantially higher when compared with the BHO doped samples, which can be associated with the better growth of the BSO nanorods within the YBCO lattice that was not the case for BHO. From this we can conclude, that the quality of the nanorod growth is directly linked to the value of the critical current. The nanorod growth depends on the associated microstrain, which again is connected to the oxygen deficiencies around the nanorods which suppress the superconducting properties in their vicinity [27]. Intuitively, the effect of this must be more pronounced if there are a lot of nanorods present, which also agrees with our observed results. The increasing and sharpening of the ab-peak up to 8 T also suggest high number of effective stacking faults as observed in the BF-STEM images. Vortex pinning is schematically illustrated in figure 5 in the associated pinscape for BSO nanorods.

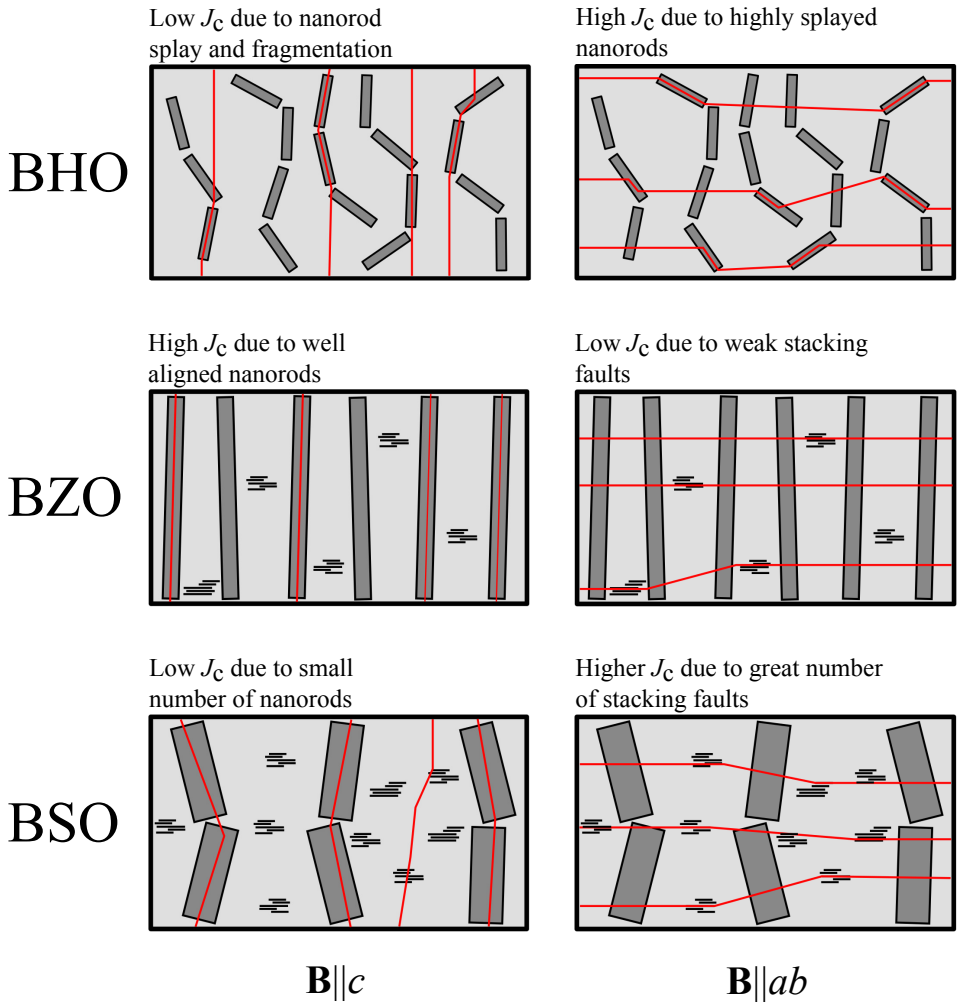

Figure 5. Schematic diagram illustrating the *c*- and *ab*-axis oriented pinning, corresponding to 0° and 90° angles, respectively, for different nanorods. The dark grey rectangles illustrate different nanorods, black horizontal lines stacking faults and red lines vortices.

4. Conclusions

We have studied the formation of pulsed laser deposited BHO, BZO and BSO nanorods within the YBCO matrix grown on an advanced IBAD-MgO based template and their effects on critical current anisotropy. The BF-TEM measurements indicate solid and *c*-axis oriented nanorod growth only in the case of BZO doped YBCO, while other nanorods are highly splayed and fragmented. Also, the diameters of the BZO and BSO nanorods are observed to be significantly smaller than in films grown on single crystalline substrates. All of these properties are explained by the increased number of lattice defects in the YBCO matrix on buffered metallic templates, which alter the strain in the YBCO between the nanorods and thus affect their formation. We also argue, that the parameters of the PLD process are more sensitive when growing a film on metallic templates than on single crystalline substrates. The transport properties

of the samples correlate highly with the crystalline quality of the films. Thus, the BZO doped sample was observed to be superior with its pronounced *c*-axis peaks and extremely high absolute values of critical current in comparison with the YBCO films doped with BHO and BSO.

References

[1] Foltyn S R, Civale L, MacManus-Driscoll J L, Jia Q X, Maiorov B, Wang H and Maley M 2007 *Nat. Mater.* **6** 631

[2] Goyal A, Norton D, Budai J, Paranthaman M, Specht E and Kroeger D 1996 *Appl. Phys. Lett.* **69** 1795

[3] Goyal A, Lee D F, List F A, Specht E D, Feenstra R, Paranthaman M, Cui X, Lu S W, Martin P M, Kroeger D M, Christen D K, Kang B W, Norton D P, Park C, Verebelyi D T, Thompson J R, Williams R K, Aytug T and Cantoni C 2001 *Physica C* **357-360** 903

[4] Iijima Y, Tanabe N, Kohno O and Ikeno Y 1992 *Appl. Phys. Lett.* **60** 769

[5] Iijima Y, Kakimoto K, Kimura M, Takeda K and Saitoh T 2001 *IEEE T. Appl. Supercond.* **11** 2816

[6] Tobita H, Notoh K, Higashikawa K, Inoue M, Kiss T, Kato T, Hirayama T, Yoshizumi M, Izumi T and Shiohara Y 2012 *Supercond. Sci. Technol.* **25** 062002

[7] Matsushita T, Nagamizu H, Tanabe K, Kiuchi M, Otabe E S, Tobita H, Yoshizumi M, Izumi T, Shiohara Y, Yokoe D, Kato T and Hirayama T 2012 *Supercond. Sci. Technol.* **25** 125003

[8] Maiorov B, Baily S A, Zhou H, Ugurlu O, Kennison J A, Dowden P C, Holesinger T G, Foltyn S R and Civale L 2009 *Nat. Mater.* **8** 398–404

[9] MacManus-Driscoll J L, Foltyn S R, Jia Q X, Wang H, Serquis A, Civale L, Maiorov B, Hawley M E, Maley M P and Peterson D E 2004 *Nat. Mater.* **3** 439

[10] Malmivirta M, Rijckaert H, Paasonen V, Huhtinen H, Hynninen T, Jha R, Awana V S, Driessche I V and Paturi P 2017 *Sci. Reports* **7** 14682

[11] Varanasi C V, Barnes P N, Burke J, Brunke L, Maartense I, Haugan T J, Stinzianni E A, Dunn K A and Haldar P 2006 *Supercond. Sci. Technol.* **19** L37–L41

[12] Varanasi C V, Burke J, Brunke L, Wang H, Sumption M and Barnes P N 2007 *J. Appl. Phys.* **102** 063909

[13] Aye M M, Khan M Z, Rivasto E, Tikkanen J, Huhtinen H and Paturi P 2019 *IEEE T. Appl. Supercond.* **29** 8000805

[14] Wu J and Shi J 2017 *Supercond. Sci. Technol.* **30** 103002

[15] Shi J J and Wu J Z 2015 *J. Appl. Phys.* **118** 164301:1–7

[16] Malmivirta M, Yao L, Huhtinen H, Palonen H, van Dijken S and Paturi P 2014 *Thin Solid Films* **562** 554–560

[17] Khan M Z, Zhao Y, Wu X, Malmivirta M, Huhtinen H and Paturi P 2018 *Physica C* **545** 50–57

[18] Khan M Z, Zhao Y, Wu X, Jha R, Awana V, Huhtinen H and Paturi P 2019 *IEEE T. Appl. Supercond.* **29** 8002105

[19] Khan M Z, Rivasto E, Wu Y, Zhau Y, Chen C, Zhu J, Palonen H, Tikkanen J, Huhtinen H and Paturi P 2019 *J. Phys. Conf. Ser. (submitted)*

[20] Rao C N R, Nagarajan R and Vijayaraghavan R 1993 *Supercond. Sci. Technol.* **6** 1–22

[21] Palonen H, Huhtinen H, Shakhov M A and Paturi P 2013 *Supercond. Sci. Technol.* **26** 045003:1–5

[22] Paturi P, Malmivirta M, Hynninen T and Huhtinen H 2018 *J. Phys. Cond. Mat.* **30** 315902:1–7

[23] Rivasto E, Khan M Z, Malmivirta M, Rijckaert H, Aye M M, Hynninen T, Huhtinen H, Driessche I V and Paturi P *Sci. Reports (submitted)*

[24] Kromann R, Bilde-Sørensen J B, de Reus R, Andersen N H, Vase P and Freltoft T 1992 *J. Appl. Phys.* **71** 3419–3426

[25] Svetchnikov V, Pan V, Træholt C and Zandbergen H 1997 *IEEE T. Appl. Supercond.* **7** 1396–1398

[26] Khan M Z, Rivasto E, Tikkanen J, Rijckaert H, Malmivirta M, Liedke M O, Butterling M, Wagner A, Huhtinen H, Driessche I V and Paturi P 2019 *Sci. Reports* **9** 15425
[27] Cantoni C, Gao Y, Wee S H, Specht E D, Gazquez J, Meng J, Pennycook S J and Goyal A 2011 *ACS Nano* **5** 4783–4789